

Multi-fidelity emulator for large-scale 21 cm lightcone images: a few-shot transfer learning approach with generative adversarial network

KANGNING DIAO ^{1,2} AND YI MAO ¹

¹*Department of Astronomy, Tsinghua University, Beijing 100084, China*

²*Berkeley Center for Cosmological Physics, University of California, Berkeley, CA 94720, United States*

Submitted to ApJ

ABSTRACT

Emulators using machine learning techniques have emerged to efficiently generate mock data matching the large survey volume for upcoming experiments, as an alternative approach to large-scale numerical simulations. However, high-fidelity emulators have become computationally expensive as the simulation volume grows to hundreds of megaparsecs. Here, we present a *multi-fidelity* emulation of large-scale 21 cm lightcone images from the epoch of reionization, which is realized by applying the *few-shot transfer learning* to training generative adversarial networks (GAN) from small-scale to large-scale simulations. Specifically, a GAN emulator is first trained with a huge number of small-scale simulations, and then transfer-learned with only a limited number of large-scale simulations, to emulate large-scale 21 cm lightcone images. We test the precision of our transfer-learned GAN emulator in terms of representative statistics including global 21 cm brightness temperature history, 2D power spectrum, and scattering transform coefficients. We demonstrate that the lightcone images generated by the transfer-learned GAN emulator can reach the percentage level precision in most cases on small scales, and the error on large scales only increases mildly to the level of a few tens of per cent. Nevertheless, our multi-fidelity emulation technique saves a significant portion of computational resources that are mostly consumed for generating training samples for GAN. On estimate, the computational resource by training GAN completely with large-scale simulations would be one to two orders of magnitude larger than using our multi-fidelity technique. This implies that our technique allows for emulating high-fidelity, traditionally computationally prohibitive, images in an economic manner.

Keywords: Reionization (1383) — Astrostatistics(1882) — Astrostatistics techniques(1886) — Interdisciplinary astronomy(804)

1. INTRODUCTION

The epoch of reionization (EoR; see, e.g. Morales & Wyithe 2010; Pritchard & Loeb 2012) is a critical period in the history of our universe, marking the last phase transition. Despite its importance, EoR remains mysterious due to insufficient observations. A widely accepted picture of EoR is the bubble model (e.g. Furlanetto & Oh 2016), where ionizing sources emit UV and X-ray photons, ionizing the surrounding intergalactic medium

(IGM) and creating ionized bubbles. These bubbles then expand and merge, eventually occupying the entire universe by the end of EoR (Chen et al. 2019).

Several observations have been used to probe EoR, including optical depth measurement of the cosmic microwave background (CMB; e.g. Aghanim et al. 2020), galaxy survey (e.g. Labbe et al. 2022; Naidu et al. 2022), Ly α forest (e.g. Gonzalez Morales & Dark Energy Spectroscopic Instrument Collaboration 2021), and 21 cm line (e.g. Furlanetto et al. 2006). The 21 cm line due to the hyperfine spin-flip transition of atomic hydrogen is a particularly promising tracer, since it can directly probe the state of the IGM during reionization. Many radio telescopes are ongoing or under construction to measure

Corresponding author: Kangning Diao, Yi Mao
dkn20@mails.tsinghua.edu.cn (KD), ymao@tsinghua.edu.cn (YM)

the global 21 cm signal, e.g. EDGES (Bowman et al. 2018), SARAS (Jishnu Nambissan et al. 2021; Bevins et al. 2022), or measure the spatial fluctuations of the 21 cm signal from the EoR, e.g. LOFAR (van Haarlem et al. 2013), MWA (Tingay et al. 2013), PAPER (Parsons et al. 2014), HERA (DeBoer et al. 2017), and SKA (Koopmans et al. 2015). Moreover, the SKA has the potential for making the images of the IGM through the 21 cm emission directly.

In preparation for the new era with the 21 cm imaging, many techniques have been developed to extract information from observations. Specifically, the Monte Carlo Markov chain (MCMC) method, e.g. 21CMMC code (Greig & Mesinger 2017), and likelihood-free inference (LFI; Alsing et al. 2019; Zhao et al. 2022a), e.g. 21CMDELFI-PS (Zhao et al. 2022b) and SCATTER-NET (Zhao et al. 2024), have been developed to infer reionization and astrophysical parameters from the 21 cm EoR signals. These methods require performing a large number of simulations, either for computing MCMC chains or for preparing training samples. These simulations range from the semi-numerical simulations, e.g. 21CMFAST (Mesinger et al. 2011; Murray et al. 2020), to radiative transfer simulations, e.g. THESAN (Kannan et al. 2021) and C²-RAY simulations (Friedrich et al. 2012; Hirling et al. 2023), with different levels of accuracy and computational costs. Given the large field of view of the next-generation telescopes, such as SKA and HERA, large-scale simulations are required to fully exploit the information from observations. However, all of these large-scale simulations are more or less computationally expensive, if not prohibitive. This bottleneck problem has inspired the development of emulators as an alternative approach to simulations.

Building emulators typically requires numerous training samples, which contradicts the original purpose of reducing computational costs. One possible solution is to build a data reservoir that gathers as many state-of-the-art simulations as possible. The publicly available CAMELS project (Villaescusa-Navarro et al. 2022) and the LoReLi database (Meriot & Semelin 2024) are such successes that have demonstrated their impacts on emulator building. However, this issue turns out to be particularly serious as the simulation volume grows to be larger than hundreds of megaparsecs on each side, in that high-fidelity emulators have become computationally expensive in this case. To address this issue, the concept of multi-fidelity emulation (Kennedy & O’Hagan 2000; Ho et al. 2021) has been proposed and guided the design of dataset (Yang et al. 2025). In this approach, a large number of low-fidelity simulations – i.e., low-cost with lower resolution or simpler

algorithms – are first used to train an emulator. The emulator is then calibrated with a small number of high-fidelity simulations, i.e. high-cost with higher resolution or more complicated algorithms. In this manner, the computational cost can be significantly reduced while still maintaining a reasonable output quality.

Machine learning (ML) has become a popular tool for astronomy in recent years, with diverse applications ranging from classifying models (e.g. Hassan et al. 2017, 2018), parameter inference (e.g. Shimabukuro & Semelin 2017; Gillet et al. 2019; Hassan et al. 2020; Zhao et al. 2022a), segmenting components (e.g. Sui et al. in prep) and generating images (e.g. Hassan et al. 2022). The Generative adversarial network (GAN; Goodfellow et al. 2014) has emerged as a powerful ML model for generating quality images thanks to its fast generation speed and high image quality. The GAN has been applied to the emulation of astrophysical images in previous works (e.g. Yiu et al. 2022; Tröster et al. 2019; List et al. 2019; Yoshiura et al. 2021). List & Lewis (2020) demonstrated that the GAN, together with the approximate Bayesian computation (ABC) method, can be used to accurately estimate the reionization parameters. Furthermore, Andrianomena et al. (2022) showed an emulation of multi-field images with GAN, which preserves the cross-correlations between different fields.

In this paper, we present a *multi-fidelity* emulation of large-scale 21 cm lightcone images from the EoR with GAN, as a trade-off between computational cost and emulation quality. Technically, this is achieved by applying the *few-shot transfer learning* method (e.g. Ojha et al. 2021), which allows for training a faithful GAN emulator with a limited number of samples and serves as the calibrating procedure in multi-fidelity emulation. Specifically, a GAN emulator is first trained with a large number of small-scale simulations, and then transfer-learned with only a limited number of large-scale simulations, to emulate large-scale EoR lightcone images. Our transfer-learned GAN emulator will be tested for precision in terms of several EoR statistics. As such, our GAN version of multi-fidelity emulation serves as a promising approach to generate data sets with high image quality and low computational cost.

When the manuscript of this paper was in preparation, diffusion models (Ho et al. 2020; Song et al. 2020), along with flow matching models with more general forward paths (Lipman et al. 2022), appeared recently as new models that also have the ability to generate high-quality data without adversarial training. Zhao et al. (2023) applied the diffusion model to generate the images of 21 cm brightness temperature mapping as a case study to conduct a quantitative comparison between

the denoising diffusion probabilistic model (DDPM) and StyleGAN2. While these state-of-the-art models are promising alternatives to GANs in generating accurate images, our work will present a successful example of multi-fidelity emulation of astrophysical images with GAN and therefore sheds light on such similar possible applications with other emulation techniques (e.g. the diffusion model and the flow matching model).

The remainder of this paper is organized as follows. In Section 2, we introduce our method for training a GAN emulator with limited data. In Section 3, we summarize the astrophysical model for generating the data sets. In Section 4, we evaluate our small-scale GAN model with several statistics. We assess the precision of our final objective, the large-scale GAN, in Section 5, and make concluding remarks in Section 6. We leave some technical details to Appendix A (on GAN architecture and configurations). Some of our results were previously summarized by us in a conference paper (Diao & Mao 2023).

2. GAN TRAINING VIA FEW-SHOT TRANSFER LEARNING

GAN is a type of generative model that is used to create new images based on a given data set. Among all types of generative models, GAN has the advantage of fast generation and high image quality, which makes it suitable for emulators. However, GAN may suffer from the so-called model collapsing problem, which means that the generated images lack diversity, especially when the data set size is limited. This means that GAN usually requires a large data set for training, which can be time-consuming and costly. In this work, we apply the idea of GAN few-shot transfer learning, aiming to train a GAN with as few training samples as possible, to reduce the computing resource requirement.

Our approach is a two-step process. First, we train our GAN with 120,000 small-scale images. The number of small-scale images is typically sufficient for GAN training, making our small-scale GAN immune to model collapse. We modify specific layers of small-scale GAN, making our GAN capable of generating large-scale images, i.e. creating a large-scale GAN. In the second step, we train our large-scale GAN with 320 large-scale images, with a patchy-level generator, a layer-frozen (FreezeD; Mo et al. 2020) multi-scale discriminator, and the cross-domain correspondence (CDC; Ojha et al. 2021) to maintain the model diversity. The details of our approach are given below.

2.1. *StyleGAN2*

A GAN typically consists of two parts, a generator G , and a discriminator D , both of which are deep neural

networks. The most naive form of the conditional GAN loss function is the so-called adversarial loss,

$$\mathcal{L}_{\text{adv}} = D(G(\mathbf{z}, \mathbf{c})|\mathbf{c}) - D(\mathbf{x}|\mathbf{c}). \quad (1)$$

Here, \mathbf{c} is the condition, e.g. the astrophysical parameters in our case. \mathbf{z} is a random vector that provides stochastic features. \mathbf{x} is the real image sample in our training set. The generator G is a function that outputs an emulated image with the input of a random vector \mathbf{z} and a set of astrophysical parameters \mathbf{c} . The discriminator D , given an image and the corresponding astrophysical parameters \mathbf{c} as input, makes a decision on whether the input image is real or not and empirically outputs the value of zero for the real and unity for the fake. The training objective is finding the optimal G and D models, as labeled by (G^*, D^*) , obtained by

$$(G^*, D^*) = \arg \min_G \max_D \mathbb{E}_{\mathbf{z} \sim p(\mathbf{z}), \mathbf{x} \sim p(\mathbf{x})} \mathcal{L}_{\text{adv}}. \quad (2)$$

Here $p(\mathbf{z})$ is the probability distribution of \mathbf{z} , modeled as a multivariate diagonal Gaussian distribution, and the distribution of real images $p(\mathbf{x})$ is imitated by our training set. \mathbb{E} means taking expectations over distributions. In practice, samples from $p(\mathbf{x})$ and $p(\mathbf{z})$ are used to obtain an empirical estimation of the expectation with maximum steps for D and minimum steps for G in turn (denoted by $\arg \min \max$).

In this work, we employ *StyleGAN2* (Karras et al. 2020), the second version of the state-of-the-art GAN model, as the GAN architecture. We illustrate the generator architecture in Figure 1. The discriminator is the commonly used ResNet (He et al. 2015) architecture. Our generator consists of two parts. First, a mapping network f takes the set of astrophysical parameters \mathbf{c} and a random vector \mathbf{z} and returns a style vector \mathbf{w} . Secondly, a synthesis network g uses the style vector \mathbf{w} to shift the weights in the convolution kernels, and Gaussian random noise is injected into the feature map right after each convolution to provide variations in the detail of the emulated map. The main structure of g keeps the form of progressively growing GAN, which generates the map with a poor resolution, e.g. 2×8 , and upsamples after convolutions until reaching the desired size. Our realization is publicly available in this GitHub repo¹. This architecture is interesting because it is similar to a simulation: the noise acts as the source of uncertainty, similar to the initial conditions in a simulation. The parameter \mathbf{c} determines how the features are spatially arranged.

¹ <https://github.com/dkn16/stylegan2-pytorch>, which is based on <https://github.com/rosinality/stylegan2-pytorch>.

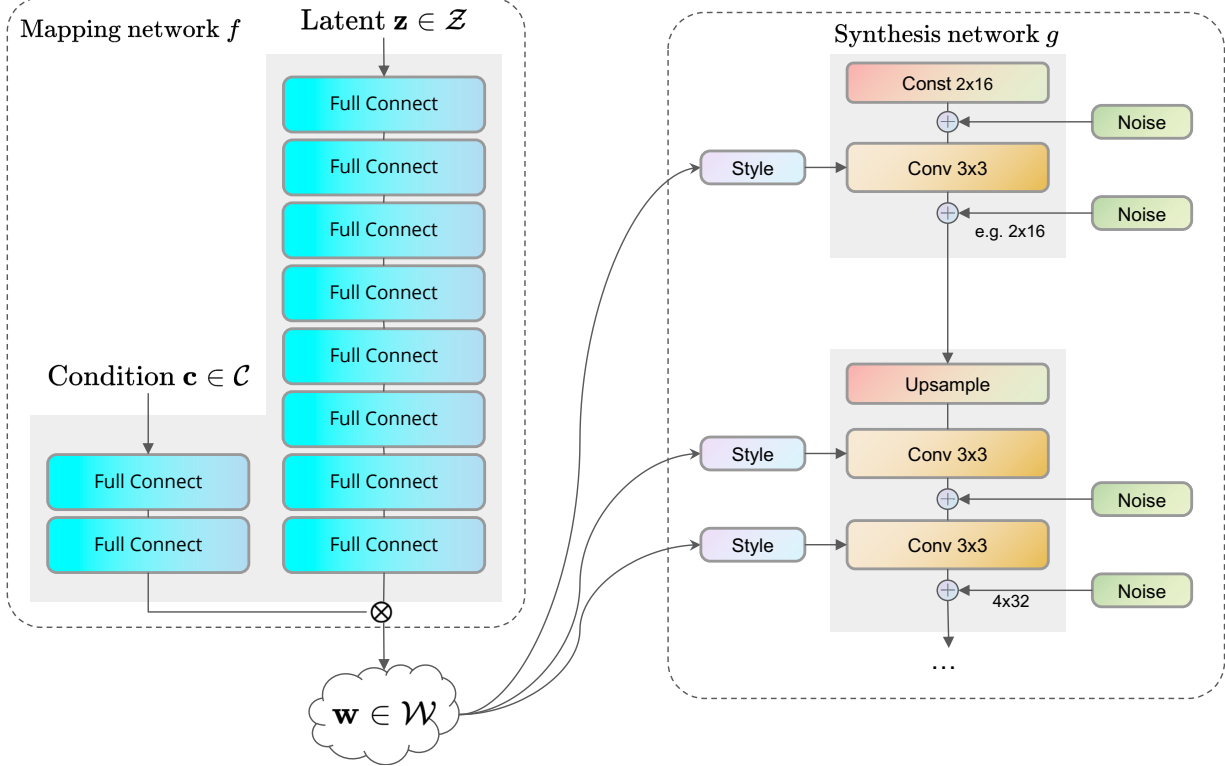


Figure 1. An illustration of the StyleGAN2 generator architecture. Our generator consists of a mapping network f , which modifies the convolution kernel according to astrophysical parameters and random vectors, and a synthesis network g , which generate images progressively, with noise injection for multiple times.

Beyond the simple form of the loss function, regularization is put on the generator and discriminator, respectively. An r_1 loss \mathcal{L}_{r_1} (Mescheder et al. 2018) is applied to the discriminator to improve the sparsity of the weight matrices, alleviating overfitting. A path-length loss is applied to the generator, which has the form of

$$\mathcal{L}_{\text{path}} = \left[\left\| \frac{\partial G(\mathbf{w})}{\partial \mathbf{w}} \right\|_2 - a \right]^2. \quad (3)$$

Here, the first term in the bracket is the change in the image caused by the change in \mathbf{w} , and $\left\| \dots \right\|_2$ denotes the 2-norm of the vector. In addition, a constant difference a in practice results in a reliable model that behaves consistently (Karras et al. 2020). Our final training objective is

$$\begin{aligned} (G^*, D^*) = & \arg \min_G \max_D \mathbb{E}_{\mathbf{z} \sim p(\mathbf{z}), \mathbf{x} \sim p(\mathbf{x})} \mathcal{L}_{\text{adv}} \\ & + \arg \min_D \mathbb{E}_{\mathbf{z} \sim p(\mathbf{z}), \mathbf{x} \sim p(\mathbf{x})} \mathcal{L}_{r_1} \\ & + \arg \min_G \mathbb{E}_{\mathbf{z} \sim p(\mathbf{z}), \mathbf{x} \sim p(\mathbf{x})} \mathcal{L}_{\text{path}}. \end{aligned} \quad (4)$$

2.2. Few-shot Transfer Learning Technique

Given a well-behaved small-scale StyleGAN2 emulator, the network structure should be modified to enable the generation of large-scale images, before retraining

it with our large-scale data set. We adopt a simple approach where we expand the size of the generator’s first layer, the CONSTANT INPUT layer, from (2, 2, 16) to (2, 8, 16) by duplicating the original layer four times and concatenating them in the second axis. Consequently, after five rounds of upsampling, the final output size is (2, 256, 512).

We then retrain our GAN with large-scale images. We first employ the patchy-level discriminator and CDC as described in Ojha et al. (2021). We mark small-scale GAN as our source model G_s and large-scale GAN as the target model G_t . We compute the CDC as follows. First, we use the same batch of vector (\mathbf{z}, \mathbf{c}) feeding both G_s and G_t , and get the corresponding small-scale image $G_s(\mathbf{z}, \mathbf{c})$ and $G_t(\mathbf{z}, \mathbf{c})$. Then, the set of computed similarity $\mathbf{S}_s(\mathbf{z}, \mathbf{c})$ between any pair of images in the $G_s(\mathbf{z}, \mathbf{c})$ sample is calculated as

$$\mathbf{S}_s(\mathbf{z}, \mathbf{c}) = \{\cos(G_s(z_i, c_i), G_s(z_j, c_j))\}_{\forall i \neq j}, \quad (5)$$

and the set of computed similarity $\mathbf{S}_t(\mathbf{z}, \mathbf{c})$ from the $G_t(\mathbf{z}, \mathbf{c})$ sample is

$$\mathbf{S}_t(\mathbf{z}, \mathbf{c}) = \{\cos(G_t(z_i, c_i), G_t(z_j, c_j))\}_{\forall i \neq j}. \quad (6)$$

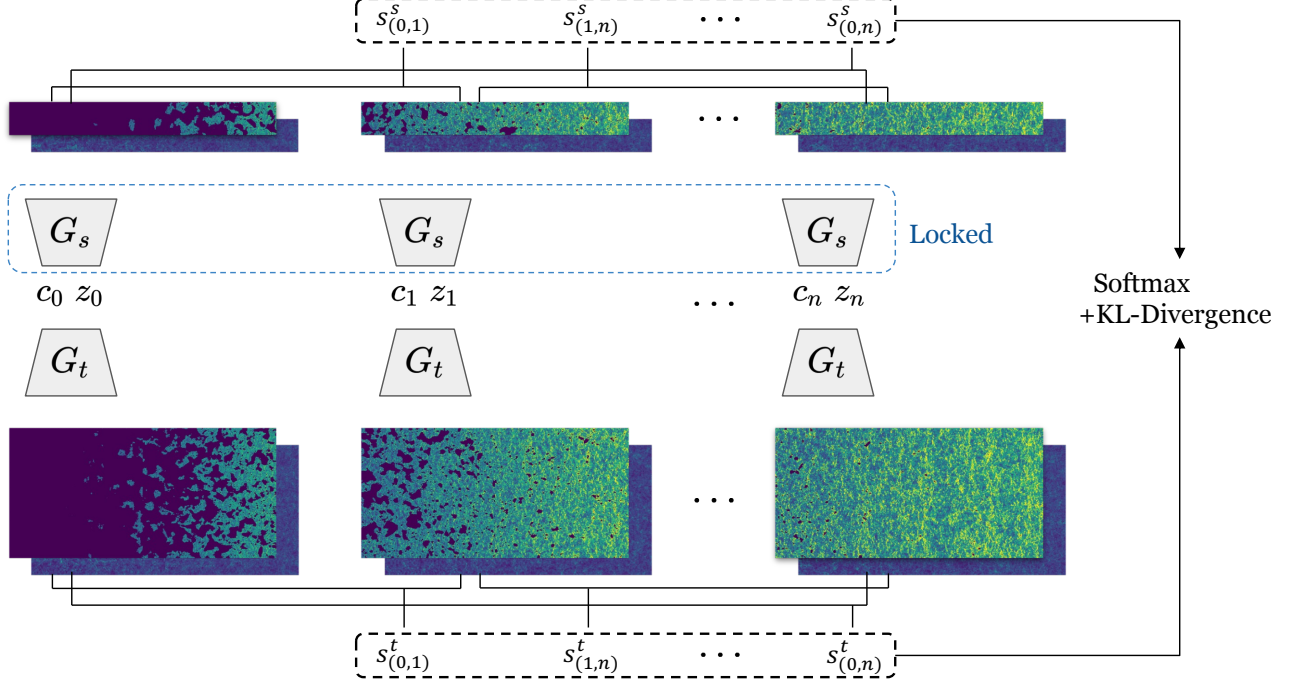


Figure 2. An illustration of CDC. We generate a set of samples with both small-scale GAN and large-scale GAN, calculate the similarity between each image pair generated by the same GAN, normalize the similarity vector of each GAN with softmax, and compute the KL-divergence as the CDC.

Here “cos” denotes the cosine similarity. Next, we normalize these two vectors in terms of softmax,

$$\text{softmax}(\mathbf{z})_i = \frac{e^{z_i}}{\sum_{j=1}^K e^{z_j}}, \quad (7)$$

where \mathbf{z} is the vector to be normalized and K is the length of \mathbf{z} . We further calculate the KL divergence between vectors

$$\mathcal{L}_{\text{CDC}} = D_{\text{KL}}(\text{softmax}(\mathbf{S}_s), \text{softmax}(\mathbf{S}_t)) \quad (8)$$

as the CDC loss. Figure 2 illustrates the idea of \mathcal{L}_{CDC} . This treatment encourages G_t to generate samples with a diversity similar to G_s , relieving the mode collapse problem.

In this work, a patchy-level discriminator is also adopted. Our training set consists only of 80 sets of parameters, which is not enough to cover the entire parameter space. Thus, we divided the whole parameter space into two parts: the anchor region and the rest. The anchor region is a spherical region around the training set parameters with a small radius. In this region, the GAN image $G_t(\mathbf{z}, \mathbf{c}_{\text{anch}})$ has a good training sample to compare with. Thus, we apply the full discriminator with these parameters. If \mathbf{c} is located outside the anchor region, we apply only a patch discriminator. In this case,

the discriminator does not calculate the loss of the whole image but calculates the loss of different patches of the image. In practice, we sample from the anchor region and train G_t with a fixed training epoch interval. This method reduces large-scale information usage and defers the happening time of the model collapse.

Since the small-scale information in both training sets is identical, we freeze the first two layers of the discriminator (Mo et al. 2020), as they extract small-scale information that does not need modification. In addition, we add an extra adversarial loss term with small-scale discriminator D_s ,

$$\mathcal{L}_{\text{adv},s} = D_s(G_{t,\text{cut}}(\mathbf{z}, \mathbf{c})|\mathbf{c}) - D_s(\mathbf{x}|\mathbf{c}), \quad (9)$$

to the loss function to ensure the robustness of small-scale information. $G_t(\mathbf{z}, \mathbf{c})$ is cut into small pieces $G_{t,\text{cut}}$ to fit the input size of D_s . Our implementation of these methods is publicly available in this GitHub repo².

3. DATA PREPARATION

In this section, we describe the process to generate our data set. We generate the EoR 21 cm mock

² <https://github.com/dkn16/few-shot-gan-adaptation>

signal using the semi-numerical simulation code 21CMFAST and create a training set that comprises of 30,000 small-scale simulations with a resolution of (64, 64, 512) and 80 large-scale simulations with a resolution of (256, 256, 512). The cell size for all simulations is (2 Mpc)³.

3.1. 21cmFAST Simulation

The observable for the 21 cm line is the differential brightness temperature T_b (see, e.g. Furlanetto et al. 2006; Mellema et al. 2013),

$$T_b \approx 27x_{\text{HI}}(1+\delta_m)\left(1-\frac{T_\gamma}{T_S}\right)\left(\frac{1+z}{10}\frac{0.15}{\Omega_m h^2}\right)^{1/2}\left(\frac{\Omega_b h^2}{0.023}\right) \quad (10)$$

in units of millikelvin. Here, x_{HI} is the neutral hydrogen fraction, δ_m is the matter overdensity, T_γ is the CMB temperature, and T_S is the spin temperature that characterizes the excitation status of hydrogen atoms between the hyperfine states. During EoR, the hydrogen gas was adequately heated, $T_S \gg T_\gamma$. Ω_m and Ω_b are the matter density and baryon density with respect to the critical density in the current epoch, respectively.

21CMFAST is a semi-numerical simulation code that uses the linear perturbation theory to yield initial condition, uses the second-order Lagrangian perturbation theory (2LPT; Scoccimarro 1998) to evolve the density field, and uses the excursion set theory (Furlanetto et al. 2004) to simulate the reionization process. Excursion set theory works by first generating the density field at a given redshift, then specifying the location of ionizing sources by introducing the minimum virial temperature T_{vir} , the threshold virial temperature for a halo that can host ionizing sources. With T_{vir} , sources will be assigned to high-density regions. The parameter ζ is used to describe the number of photons emitted per baryon by an ionizing source. Together with the baryon collapsed fraction f_{coll} , the total photons per unit volume emitted in a region are simply $n_b f_{\text{coll}} \zeta$. One can then calculate a spherical region with a radius of R , to see if $\zeta f_{\text{coll}} > 1$, which is the criterion for a region to be fully ionized. To determine the largest possible value of R that satisfies the criterion, an iteration from R_{mfp} , the mean free path of ionizing photons, to the cell size R_{cell} is carried out for every source. The spherical region with this radius is then marked as fully ionized. If R_{cell} does not satisfy the criterion, the partial ionized fraction x_{HI} for this cell is set to $1/\zeta$. Finally, the differential 21 cm brightness temperature T_b can be computed using Equation (10).

Our reionization parameters are the ionizing efficiency ζ and the minimum virial temperature T_{vir} .

- *Ionizing efficiency* ζ . ζ is related to the number of ionizing photons emitted by an ionizing source and is defined as $\zeta = f_{\text{esc}} f_* N_\gamma / (1 + \bar{n}_{\text{rec}})$, as a combination of several parameters which is still uncertain at high redshift (Wise & Cen 2009). Here, f_{esc} is the fraction of escaping photons from a galaxy into the IGM, f_* is the fraction of baryons that collapsed into the stars in the galaxy, N_γ is the number of photons produced per baryon in the star, and \bar{n}_{rec} is the mean recombination rate per baryon. We explored a range of $1 < \log_{10} \zeta < 2.398$.

- *Minimum virial temperature* T_{vir} . T_{vir} corresponds to the minimum mass of haloes that can host ionizing sources. This parameter implies the underlying physics of star and galaxy formation in dark matter haloes. In our data set, we set the range of T_{vir} as $4 < \log_{10} T_{\text{vir}} < 6$.

3.2. Training Data Set

Our data set consists of two parts — a small-scale data set and a large-scale data set.

The small-scale set has a resolution of (64, 64, 512). The data set for training the small-scale GAN consists of 30,000 lightcone simulations with a comoving length of (128, 128, 1024) Mpc. The third axis (z -axis) is along the line of sight (LoS), spanning a redshift range of $7.51 < z < 11.93$. Each such lightcone simulation box is concatenated by eight cubic boxes (each with different initial conditions). For each box, we run a simulation realization with a grid resolution of 64^3 in a comoving volume of (128 Mpc)³. For each redshift, we pick up the image slice at the corresponding comoving position in the corresponding cubic box at the corresponding cosmic time and load it into the lightcone simulation box. In other words, every 64 slices are in the same realization. Each lightcone simulation box in our small-scale data set takes 0.3 core hours and a memory of 1.2 GB. We include both the overdensity field and 21 cm T_b field for training. For each lightcone simulation box, we cut two slices in the x -axis and two slices in the y -axis, resulting in 120,000 lightcone images with the size of (2, 64, 512) in our small-scale data set, where the first channel is the T_b field and the second channel is the δ_m overdensity field.

The large-scale set has a resolution of (256, 256, 512). The data set for training the large-scale GAN consists of 80 lightcone simulations with a comoving length of (512, 512, 1024) Mpc. The third axis covers the same redshift range along the LoS as in the small-scale set. Each such lightcone simulation box is concatenated by two cubic boxes (each with different initial conditions).

For each box, we run a simulation realization with a grid resolution of 256^3 in a comoving volume of $(512 \text{ Mpc})^3$. We synthesize the lightcone simulation box from the realizations of cubic boxes in the similar approach to the small-scale set. Every 256 slices are in the same realization. Each lightcone simulation box in our large-scale data set takes 30 core hours and a memory of 29 GB. For each lightcone simulation box, we cut two slices on the x -axis and two slices on the y -axis, resulting in 320 lightcone images with the size of $(2, 256, 512)$ in our large-scale data set, containing both brightness temperature field and overdensity field for training.

For the training set, each lightcone simulation has a different set of reionization parameters. In both small-scale and large-scale training sets, we use the Latin Hypercube Sampling method (McKay et al. 2000) to sample the parameters, because this method ensures the homogeneity of parameter sample distribution in the parameter space. Therefore, while 30,000 lightcone simulations in the small-scale training set cover a wide range of parameter space, 80 lightcone simulations in the large-scale training set can also act as a representative set of parameters.

3.3. Test Data Set

For the test sets of both small-scale and large-scale GAN, we choose the same five sets of parameters that are equal-space sampled in the parameter space: $(\log_{10} \zeta, \log_{10} T_{\text{vir}}) = (1.35, 5.50), (1.7, 5.0), (2.05, 4.5), (1.35, 4.50)$ and $(2.05, 5.5)$. For illustration purposes, we will show the results only for the first three cases in the rest of this paper, but the conclusions made herein are generic and based on the tests with all five sets.

For the test set of small-scale GAN, we run 100 realizations of lightcone simulation boxes for each parameter set to minimize the impact of cosmic variance. For each realization, we extract 64 slices of lightcone images. So, the test set for evaluating the small-scale GAN consists of 6,400 image samples for each parameter set, or a total of 32,000 image samples for five parameter sets in a total of 500 realizations.

However, for the test set of large-scale GAN, limited by computational resources, we run only four realizations of lightcone simulation boxes for each parameter set. For each realization, we extract 256 slices of lightcone images. So, the test set for evaluating the large-scale GAN consists of 1,024 image samples for each parameter set, or a total of 5,120 image samples for five parameter sets in a total of 20 realizations.

4. SMALL-SCALE GAN PREPARATION

Our first step is training a small-scale GAN with sufficient data (i.e. 120,000 image samples from 30,000 simulations in this paper). Our training configurations are discussed in Appendix A.3. Since our training process is a two-step process, it is necessary to evaluate the output of the small-scale GAN. The test set for evaluating the small-scale GAN consists of 32,000 image samples for five parameter sets in a total of 500 realizations.

A visual comparison of our test samples, as shown in Figure 3, implies that our model reproduces the features of ionized bubbles in the T_b field and the cosmic web structures in the δ_m field. The ionized bubble size evolution is clearly visible in the GAN samples, and the density field shows a clearer web structure as redshift evolves. Furthermore, the bubble size and number density vary with reionization parameters.

4.1. Global Signal

Figure 4 presents the global T_b signal emulated with the small-scale GAN under different sets of parameters, with each parameter set calculated with 6,400 samples. The relative error ε_{rel} is defined as the average of the statistics evaluated by the GAN divided by the average of the statistics evaluated by the test set, minus 1:

$$\varepsilon_{\text{rel}} = \frac{\langle \text{Stats}_{\text{GAN}} \rangle}{\langle \text{Stats}_{\text{test}} \rangle} - 1 \quad (11)$$

Here, ‘‘Stats’’ denotes the statistics we choose to evaluate the GAN; in this case, it is the global signal. A cutoff is performed when $\text{Stats}_{\text{test}}$ is close to zero. We present three sets of parameters in this figure, each with a unique reionization history. Our GAN samples accurately reproduce the global signal, as seen in the relative error plot. We find that when $\langle T_b \rangle$ is large, the relative error can be at the subpercent level, but when $\langle T_b \rangle$ is small (so is the denominator in Equation 11), the error can reach the level of tens of percent. The 2σ scatter of the GAN result and the test set demonstrates a good agreement with each other for different sets of parameters, which implies that the GAN might be extensively applicable to a wide range of reionization parameters.

4.2. Power Spectrum

One of the most commonly studied statistics in EoR is the power spectrum (PS). In Figure 5, we show a comparison of the 2D PS between the GAN results and the test set with three sets of EoR parameters. For each parameter set, we use 6,400 GAN samples and 6,400 test samples to calculate the statistics.

We find that, not only do the mean values of the GAN results and the test set agree well with each other, but also the 2σ scatter regions overlap in each plot. This

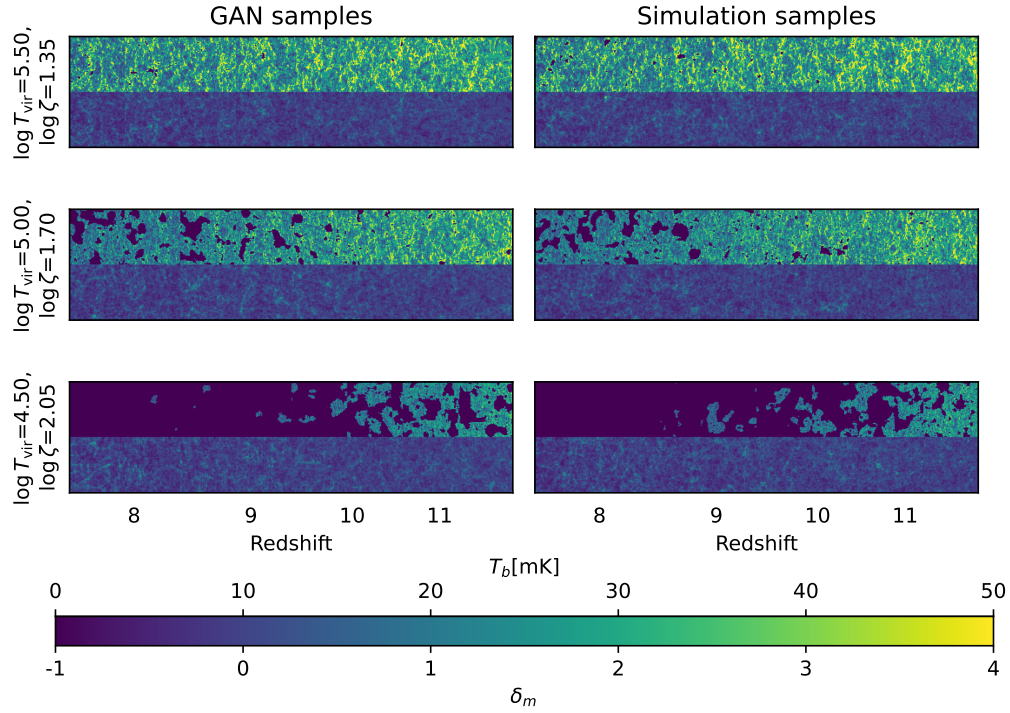


Figure 3. Examples of the emulated images using the small-scale GAN (left), in comparison with the simulated images using 21cmFAST in the test set (right). In each panel, we show the 21 cm brightness temperature (T_b) field (the upper half) and the matter overdensity (δ_m) field (the lower half). The LoS is along the x-axis.

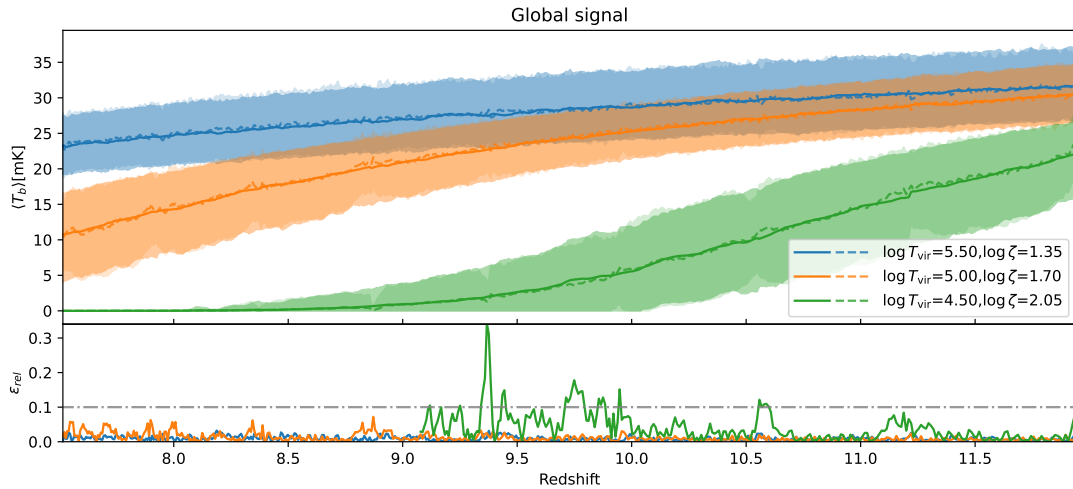


Figure 4. (Top) the global 21 cm signal emulated with the small-scale GAN, with the mean (dashed line) and 2σ scatter (shallow shaded region). We show the results with different values of reionization parameters (in different colors). Each set of reionization parameter is calculated with 6,400 image samples. For comparison, we show the results of test set images, with the mean (solid line) and 2σ scatter (thick shaded region). (Bottom) relative error between the GAN-emulated global signal and the test set. For visualization, the 10% error level is indicated with the dot-dashed line, while neglecting the data points at which the statistics for the test set are nearly zero.

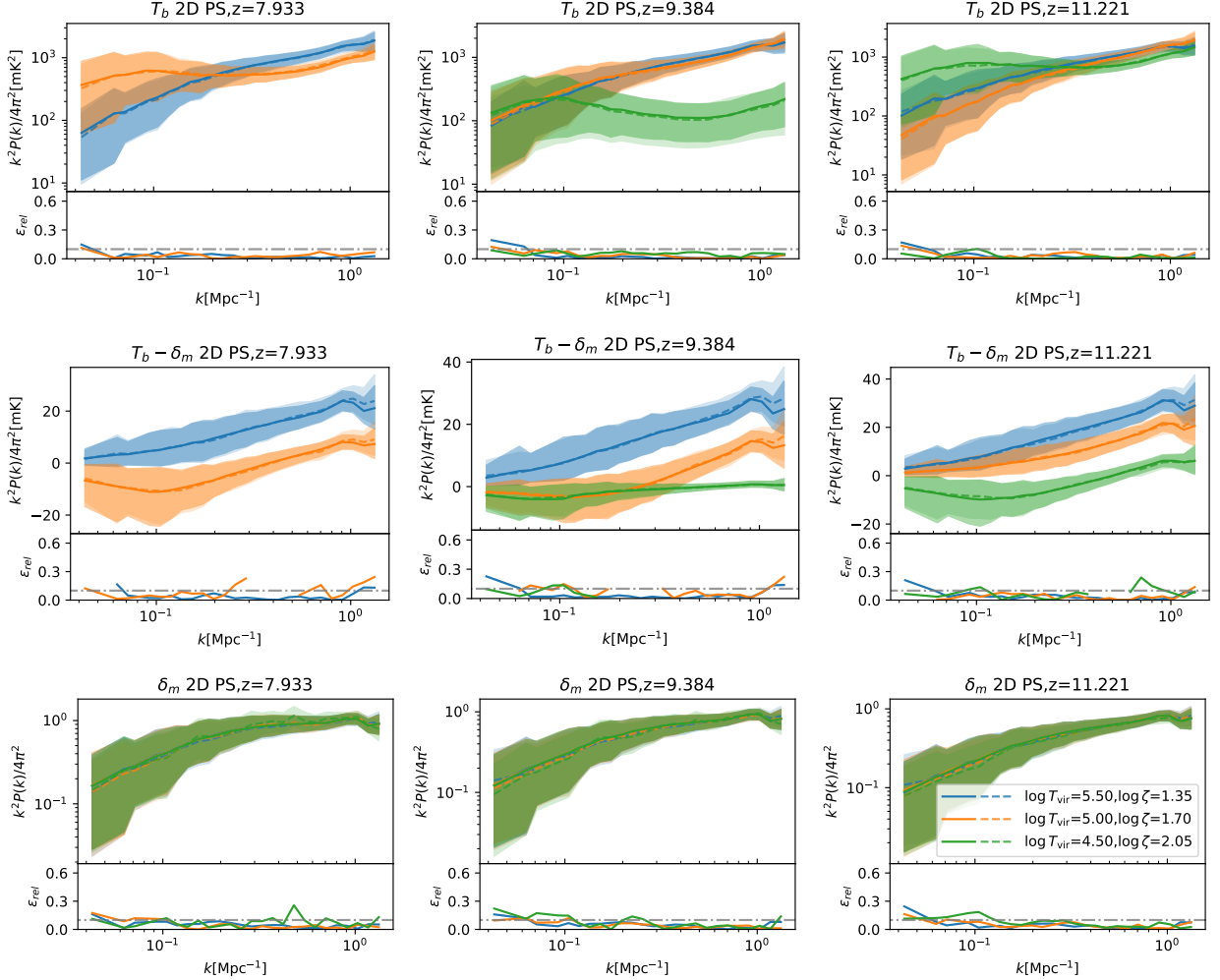


Figure 5. The 2D power spectrum of the 21 cm signal emulated with the small-scale GAN with the mean (dashed line) and 2σ scatter (shallow shaded region). We show the results with different values of reionization parameters (in different colors). Each set of reionization parameter is calculated with 6,400 clips of size (2,64,64) from the raw image. For comparison, we show the results of test set images, with the mean (solid line) and 2σ scatter (thick shaded region). From top to bottom, we show the auto-PS of the 21 cm field T_b , the cross-PS between T_b and the matter overdensity field δ_m , and the auto-PS of δ_m , respectively, at three representative redshifts of the center slice (from left to right) $z = 7.933, 9.384,$ and 11.221 . The lower sub-panel in each panel shows the relative error between the GAN-emulated PS and the test set, ϵ_{rel} . For visualization, the 10% error level is indicated with the grey dot-dashed line, while neglecting the data points at which the statistics for the test set are nearly zero. Note that the case of $(\log_{10} \zeta = 2.05, \log_{10} T_{\text{vir}} = 4.5)$ (green) is completely ionized at $z = 7.933$, so the 2D PS is not shown in the top left and middle left panels.

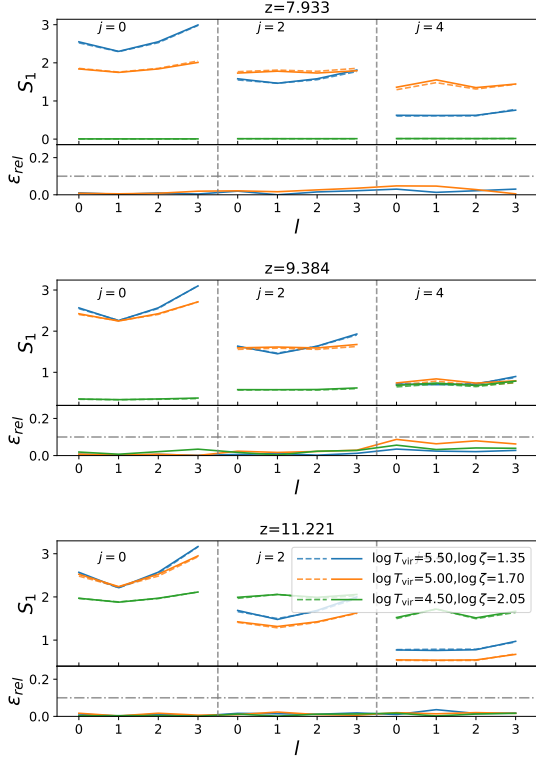


Figure 6. The ST coefficient $S_1(j, l)$ of the 21 cm signal emulated with the small-scale GAN (dashed line) and that of the test set images (solid line) at three representative redshifts of the center slice (from top to bottom) $z = 7.933$, 9.384 , and 11.221 , respectively. We show the results with different values of reionization parameters (in different colors). Each set of reionization parameter is calculated with 6,400 clips of size $(2,64,64)$ from the raw image. The lower sub-panel in each panel shows the relative error between the GAN-emulated ST and the test set, ϵ_{rel} . For visualization, the 10% error level is indicated with the grey dot-dashed line, while neglecting the data points at which the statistics for the test set are nearly zero.

agreement is observed for different sets of reionization parameters, which again supports the diversity of the GAN samples.

Our GAN performs well in recovering the correlation between fields, which is not a simple task for GAN especially when two fields have different dependencies on parameters. We find that at all stages of EoR, the relative errors of the T_b auto-PS, the δ_m auto-PS, and the T_b - δ_m cross-PS are mostly at the percent level, and overall below 20% even when the value of PS is small.

4.3. Non-Gaussianity

To capture the non-Gaussian feature beyond the PS, we employ the scattering transform (ST; e.g. Mallat 2012; Allys et al. 2019; Cheng et al. 2020; Greig et al.

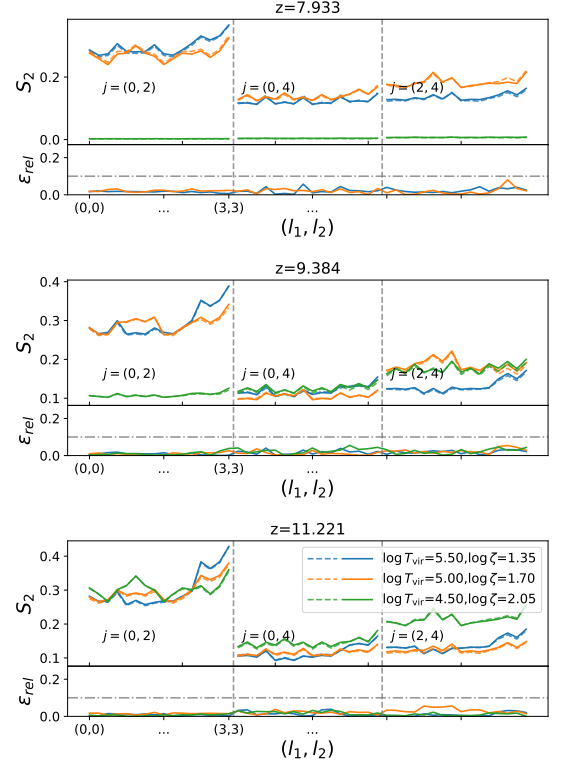


Figure 7. Same as Figure 6 but for $S_2(j_1, l_1, j_2, l_2)$. The indices (j_1, j_2) take the value of $(0, 2)$, $(0, 4)$ and $(2, 4)$. For each combination of (j_1, j_2) , the indices (l_1, l_2) run from $l_1 = 0, 1, 2, 3$ and $l_2 = 0, 1, 2, 3$, i.e. (l_1, l_2) take 16 values of $(0, 0)$, $(0, 1)$, $(0, 2)$, $(0, 3)$, $(1, 0)$, $(1, 1)$... $(3, 3)$, respectively.

2022) as a non-Gaussian statistic to evaluate our GAN. We refer interested readers to Cheng & Ménard (2021) for a detailed description of ST.

The ST coefficients S_1 and S_2 are defined as

$$\begin{aligned} I_1(j, l) &= |I_0 * \Psi(j, l)| \\ I_2(j_1, l_1, j_2, l_2) &= ||I_0 * \Psi(j_1, l_1)| * \Psi(j_2, l_2)| \\ S_1(j, l) &= \langle I_1(j, l) \rangle \\ S_2(j_1, l_1, j_2, l_2) &= \langle I_2(j_1, l_1, j_2, l_2) \rangle \end{aligned} \quad (12)$$

Here, I_0 is the input field, Ψ is the wavelet kernel (see Appendix B of Cheng et al. 2020 for its definition). The index j defines the scale of the convolutional kernel — the smaller j corresponds to a more local kernel. The index l defines the orientation of the kernel. Here we choose $j = 0, 2, 4$ and $l = 0, 1, 2, 3$ to cover a wide range of scales and orientations, resulting in 12 coefficients for $S_1(j, l)$ and 48 coefficients for $S_2(j_1, l_1, j_2, l_2)$. The ST coefficients are calculated using KYMATIO³ (Andreu et al. 2020).

³ <https://github.com/kymatio/kymatio>

We show the comparison of ST coefficients of the small-scale GAN and the test set, averaged over 6,400 samples for each parameter set, in Figure 6 (for S_1) and Figure 7 (for S_2), respectively. The GAN results show very good agreement with the test set. The relative error is mostly below 5%, and overall below 10%.

In sum, our small-scale GAN trained with 120,000 image samples that represent 30,000 sets of reionization parameters is shown to emulate the 21cmFAST simulation with high precision in both mean value and statistical scatter of several statistics. The small-scale GAN, therefore, serves as an excellent starting point for our second step, i.e. training the large-scale GAN.

5. RESULT: LARGE-SCALE GAN

Our final objective is training the large-scale GAN with a limited data set. To do so, we apply the few-shot transfer learning techniques described in Section 2.2 and generate a large-scale GAN using the small-scale GAN that was trained and tested in Section 4. We train the large-scale GAN for 2,800 epochs, using a training set that consists of only 320 image samples from 80 simulations. The test set for evaluating the large-scale GAN consists of 5,120 image samples for five parameter sets in a total of 20 realizations.

A visual inspection of the test samples of the large-scale GAN is shown in Figure 8. We find that the concatenating boundaries in the test samples of the small-scale GAN now disappear in the test samples of the large-scale GAN due to retraining, an evidence of improved image quality by our GAN.

5.1. Global Signal

Figure 9 presents the global T_b signal emulated with the large-scale GAN. Limited by the size of test set, the mean value is calculated with 1,024 image samples for each parameter set. The large-scale GAN results are slightly worse than the small-scale GAN. For example, for the case of ($\log_{10} \zeta = 2.05, \log_{10} T_{\text{vir}} = 4.5$), the relative error exceeds 10% at the early stage of reionization, and the 2σ scatter is also slightly larger than the test set. However, for the other two cases of reionization parameters, the large-scale GAN still performs well, with an error of less than 5% and a well-matched 2σ scatter region.

5.2. Power Spectrum

In Figure 10, we show a comparison of 2D PS between the large-scale GAN results and the test set. The GAN performs well on small scales, with relative error below 10%. However, on very large scales ($k \lesssim 0.02 \text{ Mpc}^{-1}$), the relative error can be $\gtrsim 30\%$. This result is not surprising because the features on large scales have not been

well trained due to very limited large-scale training sets, but given that the training set for large-scale GAN is only 320 lightcone images, this level of error is acceptable.

The 2σ scatter of the PS for the large-scale test set is much smaller than that for the small-scale test set, because more modes are included within an image sample. A similar trend is found in the GAN results, i.e. the sampling variance for the large-scale GAN is much less than that for the small-scale GAN.

5.3. Non-Gaussianity

We show the comparison of ST coefficients of the large-scale GAN and the test set in Figure 11 (for S_1) and Figure 12 (for S_2), respectively. Here we set the $j = 0, 3, 6$ to capture the large-scale information since the size of image sample is larger than in the case of small-scale GAN.

For S_1 , the relative error on small scales (i.e. small j) is small (about a few per cent), because our small-scale GAN has been well trained to provide reliable small-scale information. On the other hand, the relative error on large scales (i.e. large j) increases to $\sim 20\%$, a reasonable level of error given the very limited training set. For S_2 we find the similar trend.

5.4. Test on Mode Collapse

To assess the diversity of our large-scale GAN model, we implement several inspections, including visual inspection, pixel level variance, and feature level variance.

5.4.1. Visual inspection

We generate four realizations with the same set of reionization parameters for both GAN samples and simulation samples for visual inspection purposes, as illustrated in Figure 13. We find that the shape and size of ionized bubbles exhibit variations across different GAN samples. Furthermore, the locations of ionized bubbles also appear random, as no discernible trend or pattern is observed among the samples.

5.4.2. Pixel level variance

We show the standard deviation of the T_b field for each pixel over 1,024 image samples in Figure 14. Mode collapse would be indicated if the standard deviation in the large-scale GAN samples would be smaller than in the simulation test set. Figure 14 shows that the variances for both GAN and test set samples appear similar, particularly when T_b is large. Overall, we conclude that there is no evidence of significant mode collapse at the pixel level.

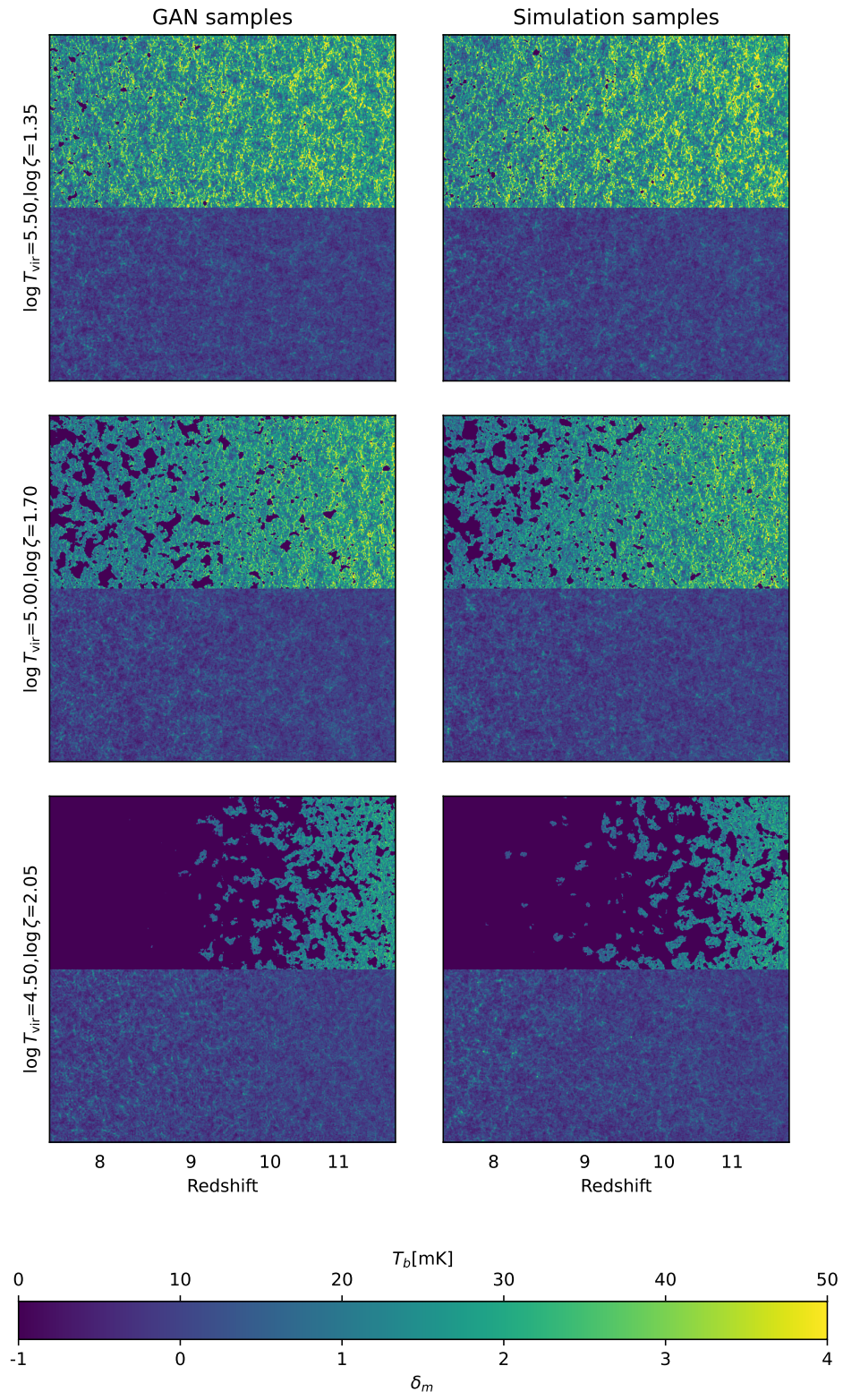


Figure 8. Same as Figure 3 but for the large-scale GAN.

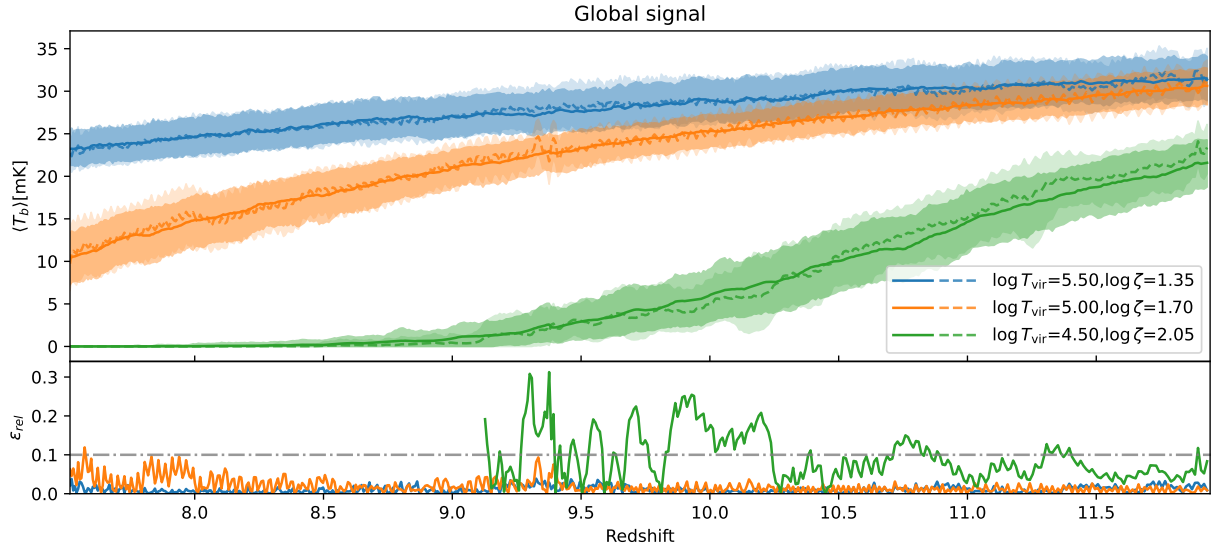


Figure 9. Same as Figure 4 but for the large-scale GAN. Each set of reionization parameter is calculated with 1,024 image samples.

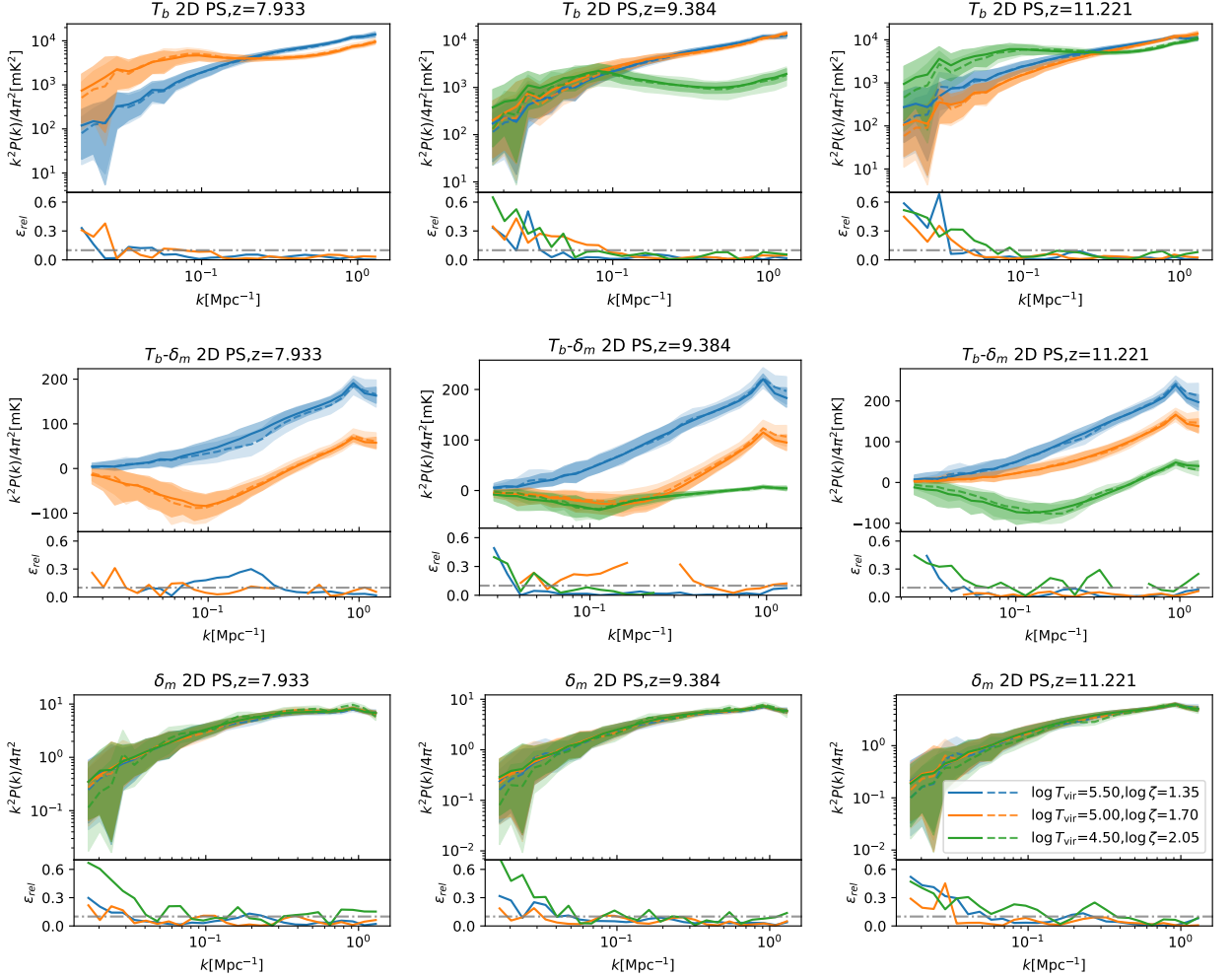


Figure 10. Same as Figure 5 but for the large-scale GAN. Each set of reionization parameter is calculated with 1,024 clips of size (2, 256, 128) from the raw image.

5.4.3. Feature level variance

We show in Figure 15 the 2σ scatter (over 1,024 image samples) of the second-order ST coefficients S_2 of the T_b field that serves as a representation of image feature. The 2σ scatter of GAN overlaps with that of simulation test set generically, indicating that there is no strong evidence of mode collapse at the feature level. The only exception is the case of $(\log_{10} \zeta, \log_{10} T_{\text{vir}}) = (2.05, 4.5)$ at $z = 9.384$ where disagreements in both the mean and 2σ scatter are found at large scales. This suggests a slight mode collapse issue in the generated images for that model at large scales at that particular redshift. Overall, the GAN samples mimic the behavior of the simulation test set quite well, except for extreme cases (e.g. when T_b is very small).

6. DISCUSSIONS AND CONCLUSIONS

In this paper, we introduce the few-shot transfer learning technique as a realization of multi-fidelity emulation in ML. As an application, we build a GAN emulator for the large-scale 21 cm lightcone images. The multi-fidelity emulation involves a two-step process — (1) building a StyleGAN2 emulator for small-scale images and training it with a huge number of training samples, and (2) modifying the model architecture to generate large-scale images and retraining the model with a limited number of training samples.

Regarding computational cost, our multi-fidelity approach allows for building a large-scale GAN emulator with the cost of one to two orders of magnitude smaller than the naive GAN approach. Specifically, the training set in our paper comprises 120,000 image samples from 30,000 small-scale simulations and 320 image samples from 80 large-scale simulations, in a total of 11,400 CPU core hours for computational cost. If we were to

Table 1. Precision and Computational Cost for Various Methods

Method	Relative Error		Computational Cost ^b
	At small scales	At large scales	[$\times 10^4$ CPU core hours]
Small-scale GAN	< 10%	—	1
Large-scale GAN (estimated ^a)	< 10%	< 10%	15 – 90
Large-scale GAN with few-shot transfer learning (this work)	< 10%	20% – 30%	1.14

^aLarge-scale GAN is training GAN only with large-scale image samples from large-scale simulations, so its performance on precision and cost is estimated here.

^bThe computational cost here includes only the bottleneck cost in generating the data set, while the cost for training the GAN is cheap and not included in the table. For example, it only took us for 320 (10) GPU card hours to train the small-scale GAN (large-scale GAN with few-shot transfer learning) with four (two) GPU cards of Nvidia Tesla V100.

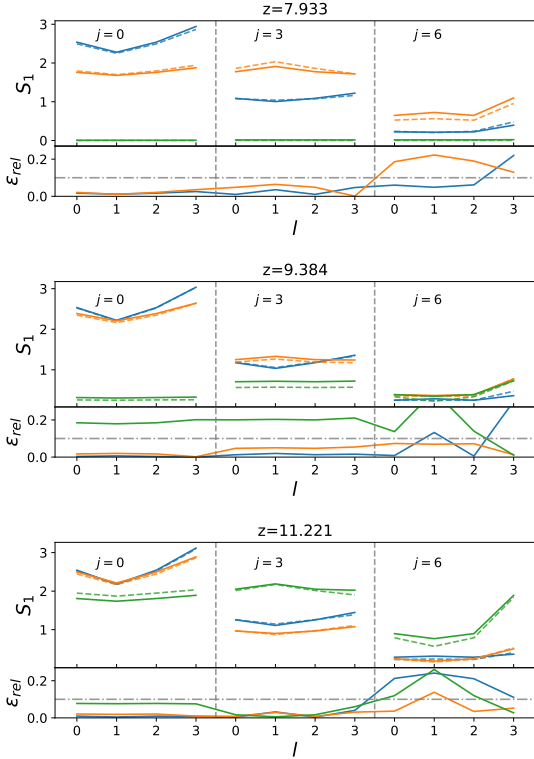


Figure 11. Same as Figure 6 but for the large-scale GAN and a choice of the index $j = 0, 3, 6$. Each set of reionization parameter is calculated with 1,024 clips of size (2, 256, 128) from the raw image.

build an emulator completely with training samples from large-scale simulations, it is estimated that at least 5,000 large-scale simulations would be required for training with about 150,000 CPU core hours. If for fair comparison purposes using the same amount of simulations to our paper, 30,000 large-scale simulations would cost 900,000 CPU core hours, about two orders of magnitude larger than our multi-fidelity approach.

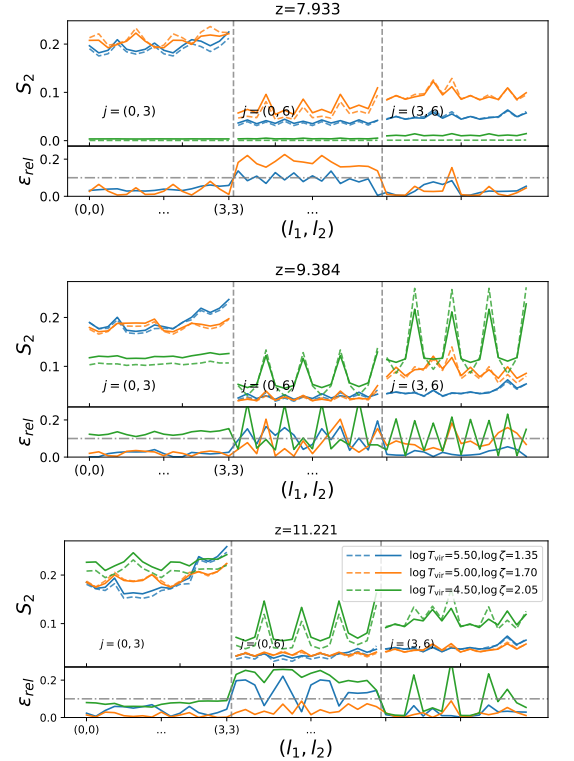


Figure 12. Same as Figure 7 but for the large-scale GAN and a choice of the index (j_1, j_2) taking the value of (0, 3), (0, 6) and (3, 6). Each set of reionization parameter is calculated with 1,024 clips of size (2, 256, 128) from the raw image.

Regarding precision, our small-scale GAN emulates small-scale images with high precision, e.g. relative error generically less than 10% for PS and 5% for ST coefficients, and our large-scale GAN emulates large-scale images with reasonable precision, e.g. relative error $\gtrsim 30\%$ on very large scales $k \lesssim 0.02 \text{ Mpc}^{-1}$ for PS and $\sim 20\%$ on large scales for ST coefficients, and on small scales

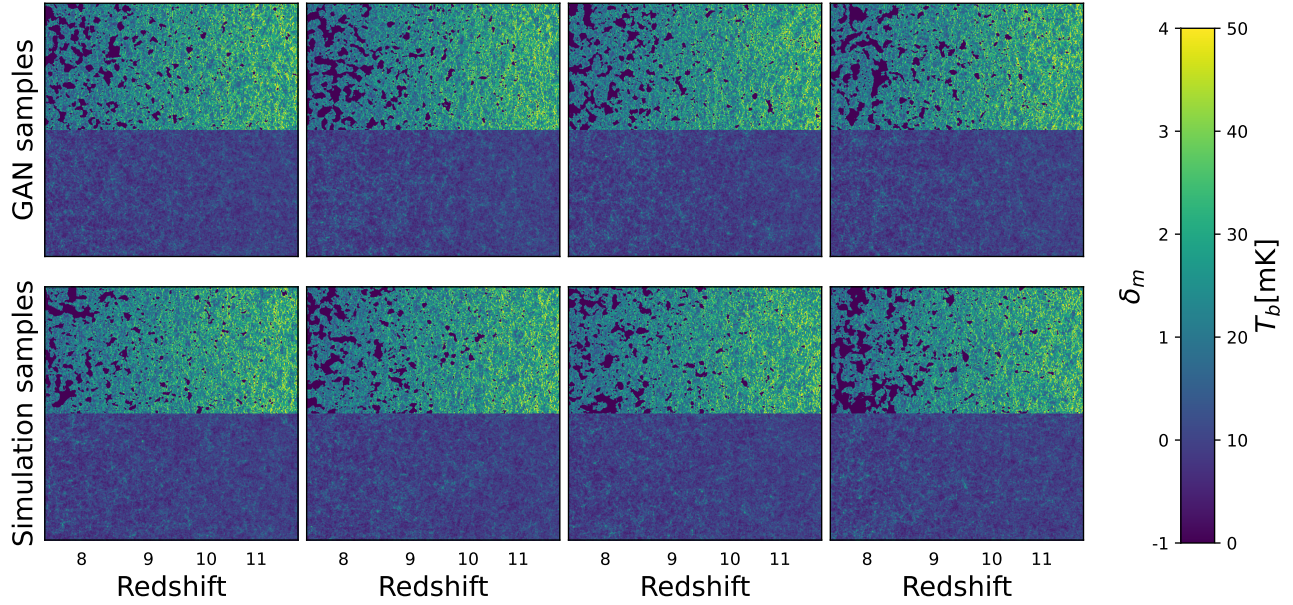


Figure 13. Visualization of the emulated images using the large-scale GAN (top), in comparison with the simulated images using 21cmFAST (bottom). Here we show four different realizations with the same parameters ($\log_{10} \zeta, \log_{10} T_{\text{vir}} = (1.7, 5.0)$). Each realization was computed using a different latent vector (for GAN) or initial condition (for simulation). In each panel, we show the 21 cm brightness temperature (T_b) field (the upper half) and the matter overdensity (δ_m) field (the lower half). The LoS is along the x-axis.

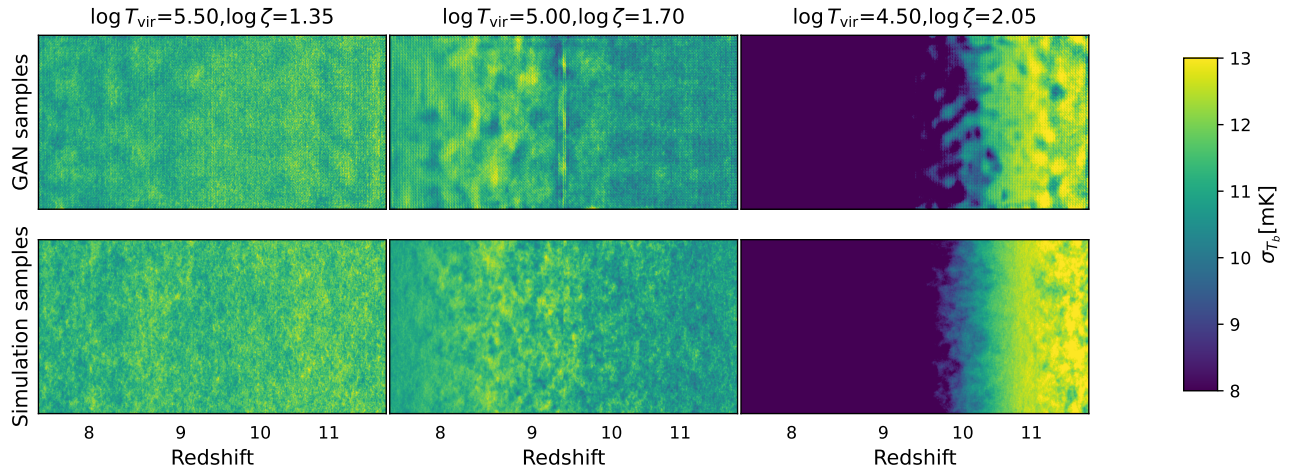


Figure 14. The standard deviation of the 21 cm brightness temperature map for each pixel over 1,024 image samples of the large-scale GAN (top), in comparison with the simulated images using 21cmFAST (bottom).

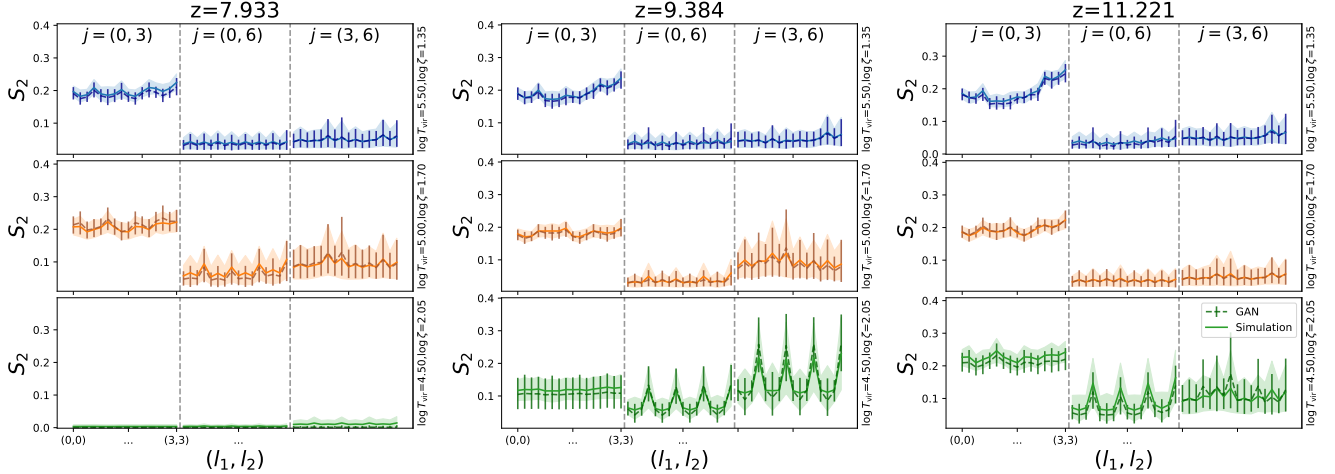


Figure 15. The 2σ scatter of the ST coefficient $S_2(j_1, l_1, j_2, l_2)$ of the 21 cm signal emulated with the large-scale GAN (dashed line for the mean and error bar for 2σ scatter) and that of the simulation test set images (solid line for the mean and shaded region for 2σ scatter) over 1,024 image samples at three representative redshifts of the center slice (from left to right) $z = 7.933$, 9.384, and 11.221, respectively. We show the results with different values of reionization parameters (in different colors and rows). The indices (j_1, j_2) take the value of (0, 3), (0, 6) and (3, 6).

with similar high precision to the small-scale GAN emulator.

We summarize the precision and computational cost in Table 1. In conclusion, our multi-fidelity approach can save 90% – 99% computational cost in emulating high-quality images with reasonable precision. This implies that the few-shot transfer learning technique allows for emulating high-fidelity, traditionally computationally prohibitive, images in an economic manner. In principle, the application can be any two sets of highly correlated image training samples in low fidelity and high fidelity, respectively, e.g. small versus large scales (this work), low versus high resolutions, semi-numerical versus full-numerical simulations.

Note that some techniques herein can be further improved. Few-shot transfer learning may be realized by other techniques, e.g. based on mutual information or style vector CDC. Also, our multi-fidelity emulation may be applied to other generative models, e.g. normalizing flow, variational autoencoder, and diffusion model. We

leave it to future work to explore other technical possibilities of multi-fidelity emulation.

ACKNOWLEDGEMENTS

This work is supported by the National SKA Program of China (grant No. 2020SKA0110401) and NSFC (grant No. 11821303). We thank Xiaosheng Zhao, Ce Sui, and Richard Grumitt for inspiring discussions. We acknowledge the Tsinghua Astrophysics High-Performance Computing platform at Tsinghua University for providing computational and data storage resources that have contributed to the research results reported within this paper.

Software: PyTorch, 21cmFAST (Mesinger et al. 2011; Murray et al. 2020), Kymatio (Andreux et al. 2020), Matplotlib (Hunter 2007), numpy (Harris et al. 2020)

APPENDIX

A. DETAILS OF GAN ARCHITECTURE AND TRAINING CONFIGURATIONS

In this appendix, we present the network structure in detail.

A.1. Generator

For our small-scale GAN, as described in Section 2, the generator consists of a mapping network f and a syn-

thesis network g . The mapping network f is constructed by two multi-layer perceptions (MLP). One MLP is an eight-layer one f_1 , mapping a Gaussian random vector \mathbf{z} to a vector of length 512: $f_1(\mathbf{z})$. The other MLP is a two-layer MLP f_2 , mapping astrophysical parameter \mathbf{c} to a 256-length vector $f_2(\mathbf{c})$. Then half of the components in the $f_1(\mathbf{z})$ are multiplied by $f_2(\mathbf{c})$ to form the final style vector \mathbf{w} . For the synthesis network g ,

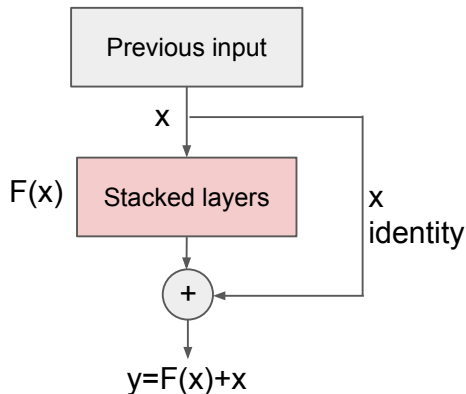


Figure 16. An illustration of a ResNet block.

it starts from a fixed layer of the size (512, 2, 16), then convolved twice before a two-times upsampling. Right after each convolution, Gaussian noise of the same size is injected into the feature map. After five times of upsampling, the feature map increases from size (512, 2, 16) to (256, 64, 512), and the reduction in channels is to save memory usage. Before each upsampling, an additional convolution layer converts the current feature map to a final image with the corresponding size, e.g. before the first convolution, the layer converts the feature map of size (512, 2, 16) to a pre-final image of size (2, 2, 16). By upsampling all pre-final images to the final size and adding them together, we obtain the final output image of size (2, 64, 512).

The style vector \mathbf{w} shapes the convolutional weights as follows. The convolution kernel can be expressed by a 4-dimensional tensor k_{ijkl} , where i is the input channel, j is the output channel, k and l are spatial indices. The

tensor k_{ijkl} is normalized with the style vector \mathbf{w} ,

$$\begin{aligned} k'_{ijkl} &= \mathbf{w}_i \cdot k_{ijkl}, \\ k''_{ijkl} &= k'_{ijkl} / \sqrt{\sum_{i,k,l} k'_{ijkl}{}^2 + \epsilon}, \end{aligned} \quad (\text{A1})$$

where ϵ is a small number to avoid numerical error.

A.2. Discriminator

The discriminator is constructed using an input layer, five ResNet blocks, and a two-layer MLP. We illustrate a ResNet block in Figure 16. The input data is added to the result of the stacked layers that is the input of the next layer. In our settings, each block has two convolution layers as the stacked layer in this block. Between each ResNet block, we downsample the feature map by a factor of two. For the small-scale GAN, after five ResNet blocks, the spatial dimension of the feature map drops from (64, 512) to (4, 32). Then the map is flattened to be a long vector. The MLP has two inputs — the long vector and astrophysical parameters, and its output is a score for which zero means real and unity means fake.

A.3. Training configurations

For the small-scale GAN, we employ four GPU cards of Nvidia Tesla V100. The training involves 40,000 iterations, with a batch size of 32 in each card, in a total of approximately 320 GPU card hours.

For the large-scale GAN, we employ two GPU cards of Nvidia Tesla V100. We run the training for 4,000 iterations with a batch size of four in each card, and find that 2,800 iterations reach the optimal performance. The cost for training the large-scale GAN is approximately 10 GPU card hours.

The hyperparameters we choose can be found in our GitHub repo.

REFERENCES

- Aghanim, N., Akrami, Y., Arroja, F., et al. 2020, *A&A*, 641, A1, doi: [10.1051/0004-6361/201833880](https://doi.org/10.1051/0004-6361/201833880)
- Allys, E., Levrier, F., Zhang, S., et al. 2019, *A&A*, 629, A115, doi: [10.1051/0004-6361/201834975](https://doi.org/10.1051/0004-6361/201834975)
- Alsing, J., Charnock, T., Feeney, S., & Wandelt, B. 2019, *MNRAS*, doi: [10.1093/mnras/stz1960](https://doi.org/10.1093/mnras/stz1960)
- Andreux, M., Angles, T., Exarchakis, G., et al. 2020, *Journal of Machine Learning Research*, 21, 1. <http://jmlr.org/papers/v21/19-047.html>
- Andrianomena, S., Villaescusa-Navarro, F., & Hassan, S. 2022, arXiv e-prints, arXiv:2211.05000. <https://arxiv.org/abs/2211.05000>
- Bevins, H. T. J., Fialkov, A., de Lera Acedo, E., et al. 2022, *Nature Astronomy*, 6, 1473, doi: [10.1038/s41550-022-01825-6](https://doi.org/10.1038/s41550-022-01825-6)
- Bowman, J. D., Rogers, A. E. E., Monsalve, R. A., Mozdzen, T. J., & Mahesh, N. 2018, *Nature*, 555, 67, doi: [10.1038/nature25792](https://doi.org/10.1038/nature25792)
- Chen, Z., Xu, Y., Wang, Y., & Chen, X. 2019, *ApJ*, 885, 23, doi: [10.3847/1538-4357/ab43e6](https://doi.org/10.3847/1538-4357/ab43e6)
- Cheng, S., & Ménard, B. 2021, arXiv e-prints, arXiv:2112.01288. <https://arxiv.org/abs/2112.01288>
- Cheng, S., Ting, Y.-S., Ménard, B., & Bruna, J. 2020, *MNRAS*, 499, 5902, doi: [10.1093/mnras/staa3165](https://doi.org/10.1093/mnras/staa3165)

- DeBoer, D. R., Parsons, A. R., Aguirre, J. E., et al. 2017, Publications of the Astronomical Society of the Pacific, 129, 045001, doi: [10.1088/1538-3873/129/974/045001](https://doi.org/10.1088/1538-3873/129/974/045001)
- Diao, K., & Mao, Y. 2023, in Fortieth ICML Machine Learning for Astrophysics workshop, 12
- Friedrich, M. M., Mellema, G., Iliev, I. T., & Shapiro, P. R. 2012, MNRAS, 421, 2232, doi: [10.1111/j.1365-2966.2012.20449.x](https://doi.org/10.1111/j.1365-2966.2012.20449.x)
- Furlanetto, S. R., & Oh, S. P. 2016, MNRAS, 457, 1813, doi: [10.1093/mnras/stw104](https://doi.org/10.1093/mnras/stw104)
- Furlanetto, S. R., Oh, S. P., & Briggs, F. H. 2006, Physics Reports, 433, 181, doi: [10.1016/j.physrep.2006.08.002](https://doi.org/10.1016/j.physrep.2006.08.002)
- Furlanetto, S. R., Zaldarriaga, M., & Hernquist, L. 2004, ApJ, 613, 1
- Gillet, N., Mesinger, A., Greig, B., Liu, A., & Ucci, G. 2019, MNRAS, 484, 282, doi: [10.1093/mnras/stz010](https://doi.org/10.1093/mnras/stz010)
- Gonzalez Morales, A., & Dark Energy Spectroscopic Instrument Collaboration. 2021, in APS Meeting Abstracts, Vol. 2021, APS April Meeting Abstracts, Z08.001
- Goodfellow, I. J., Pouget-Abadie, J., Mirza, M., et al. 2014, arXiv e-prints, arXiv:1406.2661. <https://arxiv.org/abs/1406.2661>
- Greig, B., & Mesinger, A. 2017, Proceedings of the International Astronomical Union, 12, 18, doi: [10.1017/s1743921317011103](https://doi.org/10.1017/s1743921317011103)
- Greig, B., Ting, Y.-S., & Kurov, A. A. 2022, arXiv e-prints, arXiv:2207.09082. <https://arxiv.org/abs/2207.09082>
- Harris, C. R., Millman, K. J., van der Walt, S. J., et al. 2020, Nature, 585, 357, doi: [10.1038/s41586-020-2649-2](https://doi.org/10.1038/s41586-020-2649-2)
- Hassan, S., Andrianomena, S., & Doughty, C. 2020, MNRAS, 494, 5761, doi: [10.1093/mnras/staa1151](https://doi.org/10.1093/mnras/staa1151)
- Hassan, S., Liu, A., Kohn, S., et al. 2017, Proceedings of the International Astronomical Union, 12, 47–51, doi: [10.1017/S1743921317010833](https://doi.org/10.1017/S1743921317010833)
- Hassan, S., Liu, A., Kohn, S., & Plante, P. L. 2018, MNRAS, doi: [10.1093/mnras/sty3282](https://doi.org/10.1093/mnras/sty3282)
- Hassan, S., Villaescusa-Navarro, F., Wandelt, B., et al. 2022, ApJ, 937, 83, doi: [10.3847/1538-4357/ac8b09](https://doi.org/10.3847/1538-4357/ac8b09)
- He, K., Zhang, X., Ren, S., & Sun, J. 2015, Deep Residual Learning for Image Recognition, arXiv, doi: [10.48550/ARXIV.1512.03385](https://doi.org/10.48550/ARXIV.1512.03385)
- Hirling, P., Bianco, M., Giri, S. K., et al. 2023, arXiv e-prints, arXiv:2311.01492, doi: [10.48550/arXiv.2311.01492](https://doi.org/10.48550/arXiv.2311.01492)
- Ho, J., Jain, A., & Abbeel, P. 2020, arXiv e-prints, arXiv:2006.11239, doi: [10.48550/arXiv.2006.11239](https://doi.org/10.48550/arXiv.2006.11239)
- Ho, M.-F., Bird, S., & Shelton, C. R. 2021, MNRAS, 509, 2551, doi: [10.1093/mnras/stab3114](https://doi.org/10.1093/mnras/stab3114)
- Hunter, J. D. 2007, Computing in Science & Engineering, 9, 90, doi: [10.1109/MCSE.2007.55](https://doi.org/10.1109/MCSE.2007.55)
- Jishnu Nambissan, T., Subrahmanyam, R., Somashekar, R., et al. 2021, Experimental Astronomy, 51, 193, doi: [10.1007/s10686-020-09697-2](https://doi.org/10.1007/s10686-020-09697-2)
- Kannan, R., Garaldi, E., Smith, A., et al. 2021, MNRAS, 511, 4005, doi: [10.1093/mnras/stab3710](https://doi.org/10.1093/mnras/stab3710)
- Karras, T., Laine, S., Aittala, M., et al. 2020, in Proc. CVPR
- Kennedy, M., & O’Hagan, A. 2000, Biometrika, 87, 1, doi: [10.1093/biomet/87.1.1](https://doi.org/10.1093/biomet/87.1.1)
- Koopmans, L., Pritchard, J., Mellema, G., et al. 2015, in Proceedings of Advancing Astrophysics with the Square Kilometre Array — PoS(AASKA14) (Sissa Medialab), doi: [10.22323/1.215.0001](https://doi.org/10.22323/1.215.0001)
- Labbe, I., van Dokkum, P., Nelson, E., et al. 2022, A very early onset of massive galaxy formation, arXiv, doi: [10.48550/ARXIV.2207.12446](https://doi.org/10.48550/ARXIV.2207.12446)
- Lipman, Y., Chen, R. T. Q., Ben-Hamu, H., Nickel, M., & Le, M. 2022, arXiv e-prints, arXiv:2210.02747, doi: [10.48550/arXiv.2210.02747](https://doi.org/10.48550/arXiv.2210.02747)
- List, F., Bhat, I., & Lewis, G. F. 2019, MNRAS, 490, 3134, doi: [10.1093/mnras/stz2759](https://doi.org/10.1093/mnras/stz2759)
- List, F., & Lewis, G. F. 2020, MNRAS, 493, 5913, doi: [10.1093/mnras/staa523](https://doi.org/10.1093/mnras/staa523)
- Mallat, S. 2012, Communications on Pure and Applied Mathematics, 65, 1331, doi: <https://doi.org/10.1002/cpa.21413>
- McKay, M. D., Beckman, R. J., & Conover, W. J. 2000, Technometrics, 42, 55
- Mellema, G., Koopmans, L. V. E., Abdalla, F. A., et al. 2013, Experimental Astronomy, 36, 235, doi: [10.1007/s10686-013-9334-5](https://doi.org/10.1007/s10686-013-9334-5)
- Meriot, R., & Semelin, B. 2024, A&A, 683, A24, doi: [10.1051/0004-6361/202347591](https://doi.org/10.1051/0004-6361/202347591)
- Mescheder, L., Geiger, A., & Nowozin, S. 2018, Which Training Methods for GANs do actually Converge?, arXiv, doi: [10.48550/ARXIV.1801.04406](https://doi.org/10.48550/ARXIV.1801.04406)
- Mesinger, A., Furlanetto, S., & Cen, R. 2011, MNRAS, 411, 955, doi: [10.1111/j.1365-2966.2010.17731.x](https://doi.org/10.1111/j.1365-2966.2010.17731.x)
- Mesinger, A., Furlanetto, S., & Cen, R. 2011, MNRAS, 411, 955, doi: [10.1111/j.1365-2966.2010.17731.x](https://doi.org/10.1111/j.1365-2966.2010.17731.x)
- Mo, S., Cho, M., & Shin, J. 2020, Freeze the Discriminator: a Simple Baseline for Fine-Tuning GANs, arXiv, doi: [10.48550/ARXIV.2002.10964](https://doi.org/10.48550/ARXIV.2002.10964)
- Morales, M. F., & Wyithe, J. S. B. 2010, Annual Review of A&A, 48, 127, doi: [10.1146/annurev-astro-081309-130936](https://doi.org/10.1146/annurev-astro-081309-130936)
- Murray, S., Greig, B., Mesinger, A., et al. 2020, The Journal of Open Source Software, 5, 2582, doi: [10.21105/joss.02582](https://doi.org/10.21105/joss.02582)

- Murray, S. G., Greig, B., Mesinger, A., et al. 2020, *Journal of Open Source Software*, 5, 2582, doi: [10.21105/joss.02582](https://doi.org/10.21105/joss.02582)
- Naidu, R. P., Oesch, P. A., Setton, D. J., et al. 2022, Schrodinger’s Galaxy Candidate: Puzzlingly Luminous at $z \approx 17$, or Dusty/Quenched at $z \approx 5$?, arXiv, doi: [10.48550/ARXIV.2208.02794](https://doi.org/10.48550/ARXIV.2208.02794)
- Ojha, U., Li, Y., Lu, J., et al. 2021, arXiv e-prints, arXiv:2104.06820. <https://arxiv.org/abs/2104.06820>
- Parsons, A. R., Liu, A., Aguirre, J. E., et al. 2014, *ApJ*, 788, 106, doi: [10.1088/0004-637x/788/2/106](https://doi.org/10.1088/0004-637x/788/2/106)
- Pritchard, J. R., & Loeb, A. 2012, *Reports on Progress in Physics*, 75, 086901, doi: [10.1088/0034-4885/75/8/086901](https://doi.org/10.1088/0034-4885/75/8/086901)
- Scoccimarro, R. 1998, *MNRAS*, 299, 1097, doi: [10.1046/j.1365-8711.1998.01845.x](https://doi.org/10.1046/j.1365-8711.1998.01845.x)
- Shimabukuro, H., & Semelin, B. 2017, *MNRAS*, 468, 3869, doi: [10.1093/mnras/stx734](https://doi.org/10.1093/mnras/stx734)
- Song, Y., Sohl-Dickstein, J., Kingma, D. P., et al. 2020, arXiv e-prints, arXiv:2011.13456, doi: [10.48550/arXiv.2011.13456](https://doi.org/10.48550/arXiv.2011.13456)
- Tingay, S. J., Goeke, R., Bowman, J. D., et al. 2013, *PASA*, 30, e007, doi: [10.1017/pasa.2012.007](https://doi.org/10.1017/pasa.2012.007)
- Tröster, T., Ferguson, C., Harnois-Déraps, J., & McCarthy, I. G. 2019, *MNRAS*, 487, L24, doi: [10.1093/mnrasl/slz075](https://doi.org/10.1093/mnrasl/slz075)
- van Haarlem, M. P., Wise, M. W., Gunst, A. W., et al. 2013, *A&A*, 556, A2, doi: [10.1051/0004-6361/201220873](https://doi.org/10.1051/0004-6361/201220873)
- Villaescusa-Navarro, F., Genel, S., Anglés-Alcázar, D., et al. 2022, arXiv e-prints, arXiv:2201.01300. <https://arxiv.org/abs/2201.01300>
- Wise, J. H., & Cen, R. 2009, *ApJ*, 693, 984
- Yang, Y., Bird, S., & Ho, M.-F. 2025, arXiv e-prints, arXiv:2501.06296, doi: [10.48550/arXiv.2501.06296](https://doi.org/10.48550/arXiv.2501.06296)
- Yiu, T. W. H., Fluri, J., & Kacprzak, T. 2022, *JCAP*, 2022, 013, doi: [10.1088/1475-7516/2022/12/013](https://doi.org/10.1088/1475-7516/2022/12/013)
- Yoshiura, S., Shimabukuro, H., Hasegawa, K., & Takahashi, K. 2021, *MNRAS*, 506, 357, doi: [10.1093/mnras/stab1718](https://doi.org/10.1093/mnras/stab1718)
- Zhao, X., Mao, Y., Cheng, C., & Wandelt, B. D. 2022a, *ApJ*, 926, 151, doi: [10.3847/1538-4357/ac457d](https://doi.org/10.3847/1538-4357/ac457d)
- Zhao, X., Mao, Y., & Wandelt, B. D. 2022b, *ApJ*, 933, 236, doi: [10.3847/1538-4357/ac778e](https://doi.org/10.3847/1538-4357/ac778e)
- Zhao, X., Mao, Y., Zuo, S., & Wandelt, B. D. 2024, *ApJ*, 973, 41, doi: [10.3847/1538-4357/ad5ff0](https://doi.org/10.3847/1538-4357/ad5ff0)
- Zhao, X., Ting, Y.-S., Diao, K., & Mao, Y. 2023, *MNRAS*, 526, 1699, doi: [10.1093/mnras/stad2778](https://doi.org/10.1093/mnras/stad2778)